Journal of Materials Chemistry A

PAPER

Cite this: J. Mater. Chem. A, 2015, 3, 16057

Synthesis of nanocomposites with carbon–SnO_2 dual-shells on TiO_2 nanotubes and their application in lithium ion batteries†

Zhongtao Li, Yuankun Wang, Hongdi Sun, Wenting Wu, Mei Liu, Jingyan Zhou, Guiliang Wu and Mingbo Wu*

Received 30th April 2015
Accepted 24th June 2015

DOI: 10.1039/c5ta03186a

www.rsc.org/MaterialsA

Through the introduction of well-distributed tin oxide nanocrystals on the surface of pre-prepared TiO_2 nanotubes and carbon coating, novel TiO_2/SnO_2–C double-shell nanotubes have been synthesized. As an anode material of Li-ion batteries (LIBs), DSNTs exhibit excellent long-term cycling stability (256.0 mA h g^{-1} at 1 A g^{-1} after 710 cycles) and satisfactory rate capability, which are ascribed to the synergetic effects of a unique combination of material properties in the well-designed conductive matrix: high volume stable titanium dioxide to form a one-dimensional (1D) core section to maintain the structure, large theoretical capacity tin oxide as a functional layer to increase capacity and highly conductive carbon as a buffer layer to accelerate charging rate.

1. Introduction

The design and synthesis of high capacity and long lifespan lithium batteries (LIBs) are urgently needed to meet the increasing requirements in the fields of portable devices, electrical vehicles and hybrid electric vehicles.[1–3] Currently, commercial lithium-ion batteries predominantly use graphite as anode materials, which suffers from low capacity and somewhat safety issues, which are due to the growth of lithium dendrites during discharge/charge cycling at a low Li-intercalation potential.[4] To further improve the performance of LIBs, numerous efforts have been made toward using metal oxide (M_xO_y, M = Sn, Zn, Co, *etc.*) alternatives, which have high theoretical capacities compared to carbonaceous materials.[5–8] Unfortunately, the reversible charging/discharging process of most of these materials involves tremendous volume variation and dramatic mechanical stress, which leads to electrode disintegration (electrochemical pulverization) and rapid capacity fading.[3,21]

Among these metal oxide materials, TiO_2 is one excellent candidate for anode materials due to its low cost, eco-friendliness and particularly negligible volume expansion during the discharge–charge process, which lead to long cycle life and durability.[9] Moreover, TiO_2 exhibits a high operating voltage (>1.5 V *vs.* Li^+/Li) which avoids the growth of lithium dendrites and improves LIB safety.[10] Although TiO_2 is so attractive because of these advantages, its commercial use is still hindered. The critical problems are the poor electronic conductivity, low Li-ion diffusion ability, and intrinsically low theoretical capacity.[11,31] To overcome these problems, TiO_2 particles with various nanostructures and morphology have been developed to improve their performances, such as nanoparticles, nanowires, nanosheets and nanotubes *etc.*[12–15] Although, the electrochemistry properties of these nano-materials have been obviously improved, most of the capacities are still too low for the nano-materials to be practically applied (less than 200 mA h g^{-1} at 1 A g^{-1}).

To further increase the capacity of titania-based materials for LIB anodes, combining TiO_2 with highly conductive and theoretical capacity materials such as carbon and SnO_2 is an available route.[16,17] While SnO_2 in composite electrodes can maintain the high capacity, TiO_2 can accommodate the volume expansion and maintain the structural integrity of the electrodes, the highly conductive carbon coating on the surface could improve the composites' electronic conductivity. Considering that carbon, TiO_2 and SnO_2 materials possess complementary characteristics in LIBs, numerous strategies have been developed in the recent years to design composite nanostructured TiO_2–SnO_2–C ternary systems.[18] For instance, Li and co-workers reported mesoporous TiO_2–Sn/C core–shell microspheres with superior cycling stability and high rate performance.[19] The Chen group has synthesized a new nanostructure of SnO_2 nanoparticles (NPs) encapsulated in hollow TiO_2 nanowires with a reversible capacity of 445 mA h g^{-1} at 800 mA g^{-1}.[26]

Even various TiO_2/SnO_2 composites with 1D nanostructures have been reported, few of which had TiO_2 nanotubes as

State Key Laboratory of Heavy Oil Processing, China University of Petroleum, Qingdao 266580, China. E-mail: wumb@upc.edu.cn; Fax: +86-532-86984615; Tel: +86-532-86984615

† Electronic supplementary information (ESI) available: TGA and EDS data of the DSNTs, full range of the XPS spectrum, discharge–charge profiles of TiO_2, TiO_2–C and TiO_2–SnO_2. See DOI: 10.1039/c5ta03186a

building blocks for material preparation.[17,26] The nanotubes with hollow interiors could provide extra voids to effectively alleviate the volume change and mechanical strain derived from the repeated Li^+ insertion/extraction process. More importantly, the larger specific surface area of nanotubular materials could afford more reactive sites for electrode–electrolyte interaction and accelerate electron and ion transportation. Furthermore, coated with highly conductive carbon on the surface of 1D nanotubes with a large length/diameter ratio, the composites could be effectively cross-linked with each other to fabricate a conductive matrix.[20]

Herein, we report the synthesis of TiO_2–SnO_2/C double-shell nanotubes (namely DSNTs) *via* two hydrothermal processes, followed by one liquid phase reaction process. Urea is introduced into the reaction as a surfactant and pH regulator in the hydrothermal process to well-disperse tin oxide particles in the nanoscale, which could be adhered firmly on the surface of titanium dioxide. To prevent the aggregation of SnO_2 into large grains and to buffer volume change and structural stress, resorcinol–formaldehyde (RF) is adopted as a carbon source to form a highly electric conductive coating on the TiO_2–SnO_2 nanostructures. The unique Ti–Sn–C ternary double-shell nanostructure not only provides a large interfacial area for fast lithium insertion/extraction but also reduces the diffusion pathways for electronic and ionic transport. The as-fabricated electrodes show several desirable electrochemical features: high specific capacity, excellent cycle stability, and good rate capability. These electrodes provide a potential way to practically apply TiO_2 for next-generation LIBs.

2. Experimental section

2.1. Preparation of TiO_2 nanotubes

TiO_2 nanotubes were prepared according to previous reports with slight modifications.[22,23] In a typical synthesis, 0.4 g of commercial TiO_2 was firstly dispersed into 60 mL of aqueous solution with the aid of ultrasonication. Then, 24 g of NaOH was added, and the solutions were transferred into a Teflon-lined stainless steel autoclave with a magnetic stirrer. The autoclave was put in a silicon oil bath on a hot plate and kept at 150 °C for 24 h. The stirring rate was set at ~300 rpm. Then, the autoclave was taken out from the oil bath and naturally cooled to room temperature. The white precipitates were collected using centrifugation, and washed with deionized water and a 0.1 M HNO_3 solution several times to obtain the $H_2Ti_2O_5 \cdot H_2O$ tubes. Then, the $H_2Ti_2O_5 \cdot H_2O$ tubes were washed with DI water several times until a pH value of 7 was reached, and dried in the oven overnight ready for the following thermal treatment. Finally, the TiO_2 nanotubes were obtained after heating up the dried $H_2Ti_2O_5 \cdot H_2O$ tubes in a tube furnace to 500 °C for 2 h in air.

2.2. Preparation of TiO_2–SnO_2 core–shell nanotubes

In a 200 mL beaker, 1.8 g (30 mmoL) of urea, 240 mg of as-prepared TiO_2 nanotubes, and 0.212 g (1 mmoL) of Na_2SnO_3 were mixed with 38 mL DI water and 18 mL ethanol using ultrasonication to form a milky white suspension. After ultrasonication for 30 min, the suspension was transferred into a Teflon-lined stainless steel autoclave and kept at 180 °C for 18 h. After cooling to room temperature, the TiO_2–SnO_2 core–shell nanotubes were collected using centrifugation, washed with deionized water several times and dried in the oven.

2.3. Preparation of TiO_2–SnO_2/C double-shell nanotubes and TiO_2–C core–shell nanotubes

200 mg of TiO_2–SnO_2 core–shell nanotubes was sequentially mixed with 145 mL of distilled water, 10 mL of cetyltrimethylammonium bromide (CTAB) aqueous solution (0.01 M), 1.0 mL of ammonia aqueous solution (28 wt%), 100 mg of resorcinol, and 280 μL of formaldehyde at 50 °C. After reacting for 1 h at 50 °C, the solid product was collected using centrifugation, washed with water and ethanol, and air-dried at 80 °C for several hours. The as prepared TiO_2–SnO_2/C composites were finally calcined under an argon atmosphere at 500 °C for 2 h.

To further understand the function of RF coatings, TiO_2–C core–shell nanotubes were prepared as a control sample. In this work, TiO_2 nanotubes are adopted as the starting material and coated by RF through the same process as mentioned above.

2.4. Sample characterization

The phase purity and crystal structure of the samples were characterized by X-ray powder diffraction (XRD) using an X-ray diffractometer with Cu Kα radiation from 10–75°. Transmission electron microscopy (TEM, JEM-2100UHR, Japan, equipped for an energy dispersive X-ray spectroscopy (EDS)) and high-resolution transmission electron microscopy (HRTEM) were used to examine the morphologies, crystalline structures and element distributions of the samples. The Raman spectra were measured on a Renishaw DXR Raman spectros system with a 532 nm laser source. The elemental valences of the samples were analyzed using X-ray photoelectron spectroscopy (XPS, Thermo Scientific ESCALab250Xi).

2.5. Electrochemical measurements

The working electrodes were prepared by coating a slurry of the as-prepared samples, carbon black and a poly(vinylidene) fluoride (PVDF) binder (80 : 10 : 10 in weight ratio) dissolved in *N*-methyl-2-pyrrolidinone (NMP) onto a copper foil current collector. After coating, the as prepared working electrodes were dried at 100 °C for 10 h. The electrodes were cut into disks typically with a diameter of ~12 mm, and the active material average mass loading within the coin cells was around 1.3 mg for TiO_2, 1.3 mg for TiO_2–C, 1.7 mg for TiO_2–SnO_2, and 1.5 mg for DSNTs. Li foil was used as the counter electrode and the reference electrode. The electrolyte $LiPF_6$ (1 mol L^{-1}) was dissolved in a mixture of dimethyl carbonate (DMC) and ethylene carbonate (EC) with a volume ratio of 1 : 1. The galvanostatic method at the different charge/discharge current densities from 0.5 A g^{-1} to 5 A g^{-1} was employed to measure the electrochemical capacity and cycle life of the electrodes at room temperature using a LAND-CT2001A cycler. Cyclic

voltammograms (CV) were performed using an Ametek PAR-STAT4000 electrochemistry workstation at 0.2 mV s^{-1} within the potential range of 0.005–2.5 V.

3. Results and discussion

Fig. 1 illustrates the whole fabrication process of DSNTs, which involves three steps. Firstly, anatase TiO_2 nanotubes were synthesized using a high-temperature hydrolysis reaction and ion exchange with HNO_3, followed by calcination. Then, the outer surface of the TiO_2 nanotubes was coated with a thin layer of SnO_2 nanoparticles using another hydrothermal treatment. Finally, the as-obtained TiO_2–SnO_2 nanotubes were coated with resorcinol–formaldehyde (RF) through a solution process by reacting resorcinol with formaldehyde in the presence of ammonia and CTAB, and calcination at 500 °C to induce the carbonization of the cross-linked polymer.

The structural characteristics of the as-prepared TiO_2, TiO_2–SnO_2, and DSNTs were determined using XRD (Fig. 2). As is shown in Fig. 2a, all pronounced peaks can be indexed to the anatase TiO_2 (JCPDS card no. 21-1272, $a = b = 3.785$ Å, $c = 9.514$ Å) with high crystallinity. In Fig. 2b, the XRD profile of the TiO_2–SnO_2 nanotubes indicates the presence of both anatase TiO_2 and cassiterite SnO_2 phases in the sample. The diffraction peaks at 26.6°, 33.9°, 37.9°, 51.8°,and 65.9° correspond well to the (110), (101), (200), (211), and (301) planes of cassiterite SnO_2, respectively (JCPDS card no. 41-1445, $a = 4.738$ Å, $b = 4.738$ Å, $c = 3.187$ Å).

The SnO_2 peaks in Fig. 2b and c are broad and low, which indicate that SnO_2 nanoparticles (NPs) are very small and not well crystallized in the composites. The mean particle size of SnO_2 was calculated using Scherrer's formula as 7 nm. After RF coating and the carbonization process, the XRD data of the final product was not changed (Fig. 2c).

To further understand the product properties, Raman spectra of the TiO_2 nanotubes and DSNTs in Fig. 3a were obtained. The peaks at 143, 400, 515, and 637 cm^{-1} are characteristic of anatase TiO_2 in TiO_2 nanotubes, which is consistent with the results of XRD analysis. Moreover, the characteristic D band at ~1350 cm^{-1} and G band at ~1590 cm^{-1} are observed for the DSNTs, the intensity of the G-band is higher than that of the D-band (I_D/I_G ratio of 0.85) which revealed good graphitization of the carbon layer after heat treatment at 500 °C for 2 h under N_2.

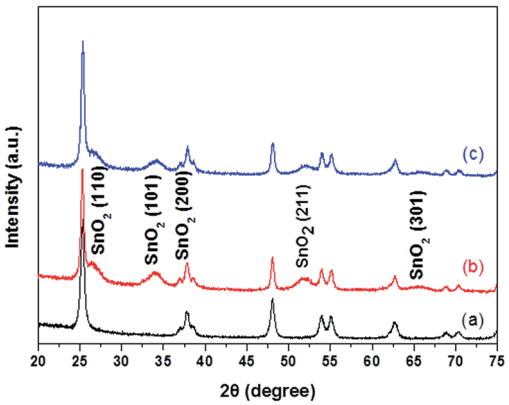

Fig. 2 XRD patterns of the as-prepared (a) TiO_2 nanotubes, (b) TiO_2–SnO_2 core–shell nanotubes, and (c) DSNTs.

To assess the thermal properties and the compositions of DSNTs, thermogravimetric analysis (TGA) was carried out in air. As shown in Fig. S1,† the major mass loss that occurred in the range of 200–600 °C can be ascribed to the combustion of the carbon coating in air. Finally, the curve of SnO_2-QDs/N-GNs tends to be horizontal; we can deduce that the carbon content is about 10.0%.

To further investigate the chemical composition and valence states of the DSNTs, XPS spectra and EDS data were obtained. The experimental data indicated that the DSNTs are composed of C, O, Ti, and Sn. The EDS data (Fig. S2†) revealed that the

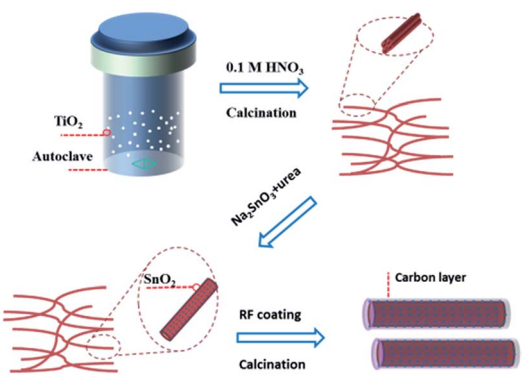

Fig. 1 Schematic illustration of the fabrication process.

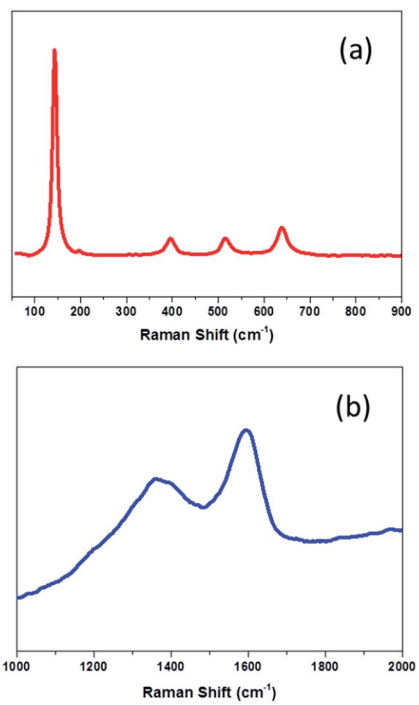

Fig. 3 Raman spectrum of the (a) TiO_2 nanotubes and (b) DSNTs.

percentages of tin and titanium in the DSNTs are 1.94 at% and 9.25 at%, respectively. But the elemental content of Sn and Ti are 3.23 at% and 6.16 at% as shown in the XPS data in Fig. S3.† The higher content of tin shown in the XPS data is due to the distribution of most of the tin oxide being on the surface of the nanotubes. In Fig. 4, the XPS results reveal the C, O, Ti, and Sn spectra of the DSNTs. The high resolution C 1s spectrum (Fig. 4a) was centered at 284.1 eV, which can be split into four components with binding energies of 284.1 eV (non-oxygenated carbon (C–C)), 284.7 eV (C_6H_6), 286.1 eV (C–O–C/C–OH), and 289.17 eV (carbonyl group (C═O)).[24] The deconvoluted peaks (Fig. 4b) of the O 1s spectrum were resolved into three components, centered at 529.9, 530.5, and 531.9 eV. The binding energy component observed at 529.9 eV and 530.5 eV is attributed to the Auger electron of O^{2-} in TiO_2 and SnO_2, while, the peak at 531.9 eV can be assigned to the C═O bonds in the carbonyl group. Fig. 4c exhibits the Ti 2p XPS spectrum, in which two distinct peaks at 464.7 eV and 458.7 eV can be assigned to Ti $2p_{1/2}$ and Ti $2p_{3/2}$ respectively, which reflect a typical signal of Ti^{4+} in an octahedral crystal.[25] The curve fitted core level spectra of Sn 3d are shown in Fig. 4d. Two peaks at 495.3 eV and 486.8 eV could be found, which correspond well to Sn $3d_{3/2}$ and Sn $3d_{5/2}$ and demonstrate the formation of SnO_2.[27]

As shown in Fig. 5, the morphologies and nanostructures of the as-prepared composites were characterized using TEM. In Fig. 5a, elongated $H_2Ti_2O_5 \cdot H_2O$ nanotubes were formed by mechanical force during the hydrothermal process, which are around 10 nm in diameter and 4.5 μm in length on average. After the first high temperature calcination, the crystalline nanotubes were transformed from $H_2Ti_2O_5 \cdot H_2O$ to anatase TiO_2 through a topotactic transformation.[25] In addition, the diameter of the nanotubes also increases after thermal annealing due to the merging of multiple parallel orientated nanotubes, as can be seen from Fig. 5b.[23] In the high resolution TEM image, a lattice spacing of 0.20 nm could be defined, which can be ascribed to the (020) planes of anatase TiO_2 (Fig. 5b(2)). The selected area electron diffraction (SAED) pattern of the TiO_2 nanotubes (Fig. 5b(1)) shows a set of well-defined dots, indicative of the single-crystallinity of anatase TiO_2. The results of HR-TEM and SAED affirm that the nanotubes prefer to grow in the (010) crystallographic direction, consistent with the findings in a previous study.[22] Fig. 5b shows the TEM images of the TiO_2–SnO_2 nanotubes. The roughness of the TiO_2–SnO_2 nanotubes is increased, which indicates the successful deposition of SnO_2 nanoparticles on the TiO_2 nanotubes, which has also been confirmed using Brunauer–Emmett–Teller (BET) N_2 adsorption–desorption analysis (Fig. S4†). The experimental data revealed that the specific surface area of TiO_2–SnO_2 increases to 94.75 $m^2\ g^{-1}$, which is 67.35 $m^2\ g^{-1}$ for pure TiO_2 tubes. The average diameter of the SnO_2 nanoparticles is approximately 7 nm, which has been approved by XRD analysis. The lattice fringes of the SnO_2 nanoparticles are measured as 0.335 nm, which are in agreement with the *d*-spacing of the (110) plane of cassiterite SnO_2, as shown in the inset of Fig. 5c. After solution processing with RF and carbonization in Ar, the carbon coating could be identified in the core–shell structure (Fig. 5d). The carbon coating layer that is around 10 nm thick, uniformly covers the surface of the TiO_2–SnO_2 nanotubes.[20] In addition, SAED patterns were recorded by focusing the electron beam on an area indicated by a square (inset of Fig. 5d), indicating that cassiterite SnO_2 and anatase TiO_2 both exist in DSNTs.

The experimental data of discharge–charge measurements of the DSNTs are shown in Fig. 6. Discharge–charge measurements were carried out at a current density of 500 mA g^{-1} between 0.005 to 2.5 V (*vs.* Li) at room temperature. The voltage *versus* capacity profiles are shown in Fig. 6a. In the discharge curve of the first cycle, there are two obvious voltage plateaus (~1.7 and 0.74 V) resulting from lithium reacting with TiO_2 and SnO_2, respectively. The first plateau at ~1.7 V is associated with the phase transition between the tetragonal TiO_2 and

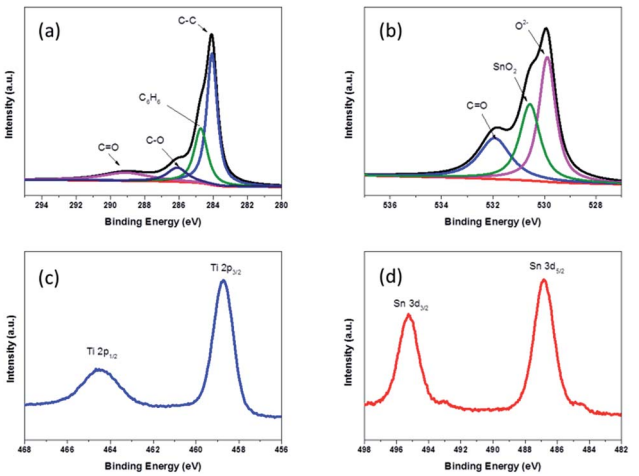

Fig. 4 XPS spectra of (a) C 1s, (b) O 1s, (c) Ti 2p and (d) Sn 3d regions of the DSNTs.

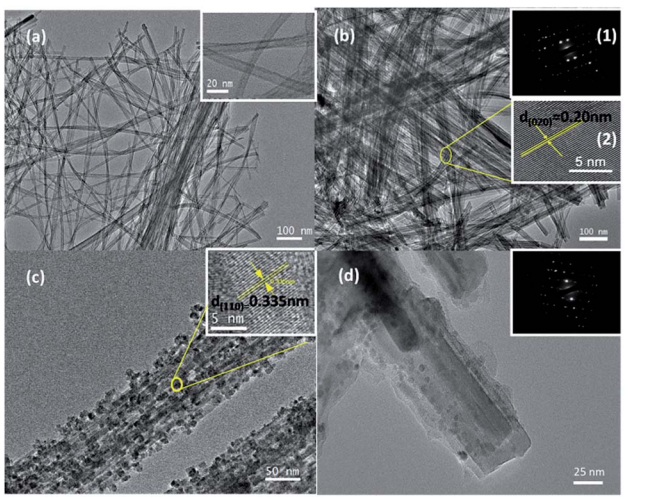

Fig. 5 (a–d) Low-magnification TEM images of the $H_2Ti_2O_5 \cdot H_2O$ nanotubes, TiO_2 nanotubes, TiO_2–SnO_2 nanotubes, and DSNTs, respectively; inset in (a), (b(2)), and (c) are high-magnification TEM images for the $H_2Ti_2O_5 \cdot H_2O$ nanotubes, TiO_2 nanotubes, and TiO_2–SnO_2 nanotubes respectively; inset in (b(1)) and (d) are SAED patterns of the TiO_2 nanotubes and DSNTs, respectively.

orthorhombic Li_xTiO_2 phase.[28,29] The second plateau at 0.74 V can be ascribed to the reaction of SnO_2 with lithium to form solid electrolyte interface (SEI) layers, which does not appear in the subsequent cycling.[30]

Similarly, the charge curve shows two plateaus at ~0.54 and 2.1 V, which can be ascribed to the lithium extraction behaviour. The Li reaction with the DSNT electrodes can be written as:

$$TiO_2 + xLi^+ + xe^- \leftrightarrow Li_xTiO_2\ (0 \le x \le 1) \quad (1)$$

$$SnO_2 + 4Li^+ + 4e^- \rightarrow Sn + 2Li_2O \quad (2)$$

$$Sn + x'Li + x'e^- \leftrightarrow Li_{x'}Sn\ (0 \le x' \le 4.4) \quad (3)$$

where x and x' are the amount of inserted Li^+ in anatase TiO_2 and SnO_2, respectively. The DSNTs yield a specific capacity on the first discharge (1166.6 mA h g^{-1}) and charge (459.1 mA h g^{-1}). The large capacity loss (~60%) in the first cycle is mainly attributed to irreversible side reactions such as the inevitable formation of SEI films and electrolyte decomposition, which are common to most lithium intercalation hosts. The voltage-capacity trace of the TiO_2, TiO_2–C and TiO_2–SnO_2 nanotubes was also recorded for comparison (Fig. S5†). In the first discharge process, the capacities gradually increased from 376.9 mA h g^{-1} of TiO_2 to 414.8 mA h g^{-1} of TiO_2–C, and finally to 1129.8 mA h g^{-1} of TiO_2–SnO_2. The increased capacity can be attributed to the combination effects of the RF coating and SnO_2. CV curves of DSNTs at a scan rate of 0.2 mV s^{-1} with cut-off voltages of 2.5–0.005 V (*versus* Li^+/Li) are shown in Fig. 6b. In the first cycle, a pair of anatase TiO_2 cathodic/anodic peaks at 1.7 and 2.1 V can be observed, which are caused by Li insertion/extraction between TiO_2 and Li (reaction (1)). Meanwhile, the irreversible cathodic peak around 0.74 V is attributed to the formation of the SEI layer, and the same voltage plateaus could be found in the discharge–charge profiles (Fig. 6a). The almost overlapping curves of the second and fifth cycle indicate highly reversible redox behaviour and good cycling stability of the DSNT electrodes.

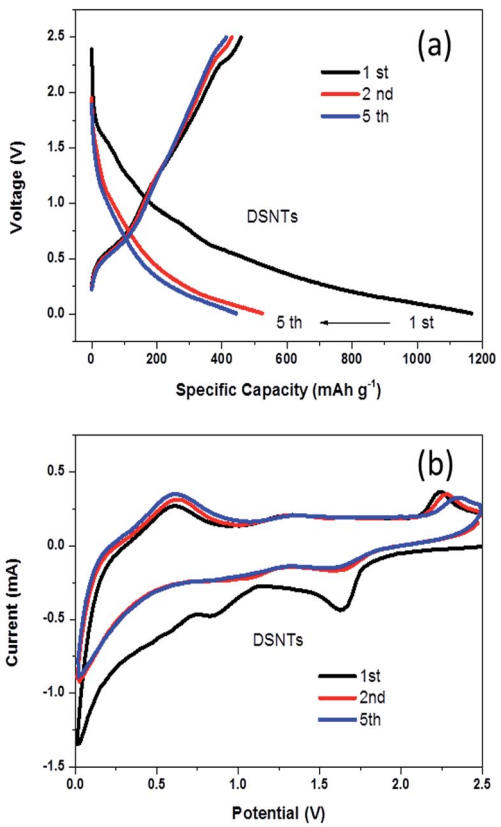

Fig. 6 (a) Discharge–charge profiles of the DSNTs at a constant current density of 500 mA g^{-1}; (b) CV curves of the DSNT anode at a 0.2 mV s^{-1} scanning rate.

Fig. 7a shows the cycling performance at a current density of 500 mA g^{-1} for the as-prepared four materials. The discharge capacities of the TiO_2, TiO_2–C, and TiO_2–SnO_2 electrodes after 120 cycles at 500 mA g^{-1} are 76.5, 80.1, and 78.5 mA h g^{-1}, respectively. The poor cycling stability of the TiO_2–SnO_2 electrodes is due to the tremendous volume changes of the SnO_2 nanoparticles.[6,30] DSNT-based electrodes delivered improved reversible charge/discharge stability and the discharge capacity remains at 354.3 mA h g^{-1} even after 120 cycles at a current density of 500 mA g^{-1}. The long-term cycling performance of the DSNTs at a current density of 1 A g^{-1} is shown in Fig. 7b. The reversible discharge capacity of the DSNT electrodes after 710 cycles is 256 mA h g^{-1}, which corresponds to 85.8% retention of the 10th discharge capacity (304.8 mA h g^{-1}). Moreover, the coulombic efficiency is almost 100% after several cycles, which indicates high reversibility of the DSNT electrodes. Such improved electrochemistry performance implies that the RF layer on the surface of the TiO_2–SnO_2 nanotubes plays an essential role in the accommodation of the metal oxide volume change and improvement of the electron conductivity. Moreover, the DSNTs also exhibit excellent rate performances as shown in Fig. 7c. Remarkably, even at a high current density of 5.0 A g^{-1}, the capacity of this lithium-ion cell can reach around 77.0 mA h g^{-1}. More importantly, the specific capacity rebounds back to 350.3 mA h g^{-1} when the current density swings back to 500 mA g^{-1}, indicating the remarkable rate capability and stability of the DSNTs. To further understand the satisfactory electrochemical performance, a TEM image of the DSNTs after 300 cycles at 1 A g^{-1} is presented in Fig. S6.† In addition to some impurities from carbon black and the binder, the 1D nanotubes in the DSNTs could be easily identified after long-term repeated lithiation/delithiation, which indicates the excellent structure stability of the DSNTs.

Fig. 7d shows the electrochemical impedance spectra (EIS) of TiO_2, TiO_2–SnO_2, and the DSNTs. The Nyquist plots of all three electrodes depict a semicircle in the high-medium frequency region, corresponding to the charge transfer resistance. An inclined line in the low frequency region represents the diffusion resistance. It is worth noting that the diameter of the semicircle for the DSNT electrodes (52.34 ohm) is much smaller than that of TiO_2 (111.1 ohm) and TiO_2–SnO_2 (212.3 ohm), which suggests that the DSNTs possess the lowest contact and charge transfer resistances. It can be attributed to the fabrication of the highly conductive matrix through the coated

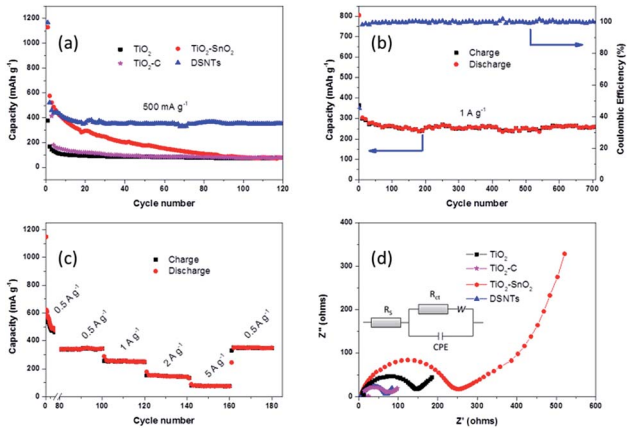

Fig. 7 (a) Cyclic performance of the TiO_2, TiO_2–C, TiO_2–SnO_2, and DSNT electrodes at a current density of 500 mA g^{-1}, (b) long-term cycling performance of the DSNTs at 1 A g^{-1}, (c) rate capacity of the DSNTs at different current densities, and (d) electrochemical impedance spectra of TiO_2, TiO_2–C, TiO_2–SnO_2 and DSNTs; the inset of (d) is the fitting circuit, R_s: ohmic resistance (total resistance of the electrolyte, separator, and electrical contacts); R_{ct}: charge transfer resistance; W: Warburg resistance; CPE: constant phase-angle element.

nanotubes, which affords effective channels for charge transfer through better connection with metal oxide particles.

The excellent cycling stability and rate capability of the DSNTs are associated with the unique combination of material properties. In the composite, volume expansion is negligible for TiO_2 tubes in the core section which maintains its high durability, and its 1D structure could effectively reduce the diffusion pathways for ionic transport; the well-defined SnO_2 nanoparticles on TiO_2 tubes could increase the lithium storage capacity. The highly conductive carbon coating has the following functions: firstly, the nanotubes could connect with each other through "touching" of the outer conductive carbon coating, which could effectively create a conductive network over the entire system. Secondly, the uniform carbon layer on the surface could alleviate the stress generated by the large volume variation in SnO_2 NPs during the repeated cycle processes to avoid their aggregation and maintain the unique double-shell nanostructure.

4. Conclusions

In summary, TiO_2/SnO_2–C double-shell nanotubes have been synthesized for high performance Li-ion battery anodes. By introducing urea as the surfactant and pH regulator during the hydrothermal process, tin oxide nanocrystals were well dispersed on the surface of the pre-prepared TiO_2 nanotubes. Thereafter, resorcinol–formaldehyde (RF) was deposited on the TiO_2–SnO_2 composite, followed by thermal treatment to form a continuous carbon layer. As ascribed to the synergetic effects of a unique combination of material properties, the double-shell nanotubes exhibit a greatly enhanced reversible capacity (256 mA h g^{-1} after 710 cycles at 1 A g^{-1}) and rate capability (77 mA g^{-1} at 5 A g^{-1}), which are greatly improved compared to that of pure TiO_2, TiO_2–C, and TiO_2–SnO_2 nanotubes. The method described in this paper may provide a simple, economic and effective strategy for the preparation of next generation LIBs.

Acknowledgements

This work is supported by the National Natural Science Foundation of China (no. 51303212, 51303202, 21302224, 51372277); National Natural Science Foundation of Shandong Province (ZR2013BQ028, ZR2013EMQ013); The Fundamental Research Fund for the Central Universities (14CX02196A, 15CX08005A, 15CX05010A) and Open Fund of Beijing National Laboratory for Molecular Sciences (2013019).

References

1 M. V. Reddy, G. V. Subba Rao and B. V. R. Chowdari, *Chem. Rev.*, 2013, **113**, 5364.
2 W. Zhang, *J. Power Sources*, 2011, **196**, 13.
3 Z. Wang and L. Zhou, *Adv. Mater.*, 2012, **24**, 1903.
4 G. Zhu, Y. Wang and Y. Xia, *Environ. Sci. Technol.*, 2012, **5**, 6652.
5 J. S. Chen, Y. L. Cheah, Y. T. Chen, N. Jayaprakash, S. Madavi, Y. H. Yang and X. W. Lou, *J. Phys. Chem. C*, 2009, **113**, 20504.
6 Z. Li, G. Wu, D. Liu, W. Wu, B. Jiang, J. Zheng, Y. Li, J. Li and M. Wu, *J. Mater. Chem. A*, 2014, **2**, 7471.
7 S. J. Yang, S. Nam, T. Kim, J. H. Im, H. Jung, J. H. Kang, S. Wi, B. Park and C. R. Park, *J. Am. Chem. Soc.*, 2013, **135**, 7394.
8 X. W. Lou, D. Deng, J. Y. Lee, J. Feng and L. A. Archer, *Adv. Mater.*, 2008, **20**, 258.
9 W. Li, F. Wang, S. Feng, J. Wang, Z. Sun, B. Li, Y. Li, J. Yang, A. A. Elzatahry, Y. Xia and D. Zhao, *J. Am. Chem. Soc.*, 2013, **135**, 18300.
10 B. Hao, Y. Yan, X. Wang and G. Chen, *ACS Appl. Mater. Interfaces*, 2013, **5**, 6285.
11 J. Liao, D. Higgins, G. Lui, C. Victor, X. Xiao and Z. Chen, *Nano Lett.*, 2013, **13**, 5467.
12 S. Bach, J. P. Pereira-Ramos and P. Willman, *Electrochim. Acta*, 2010, **55**, 4952.
13 Z. Yang, G. Du, Z. Guo, X. Yu, Z. Chen, T. Guo, N. Sharma and H. Liu, *Electrochem. Commun.*, 2011, **13**, 46.
14 S. Yang, X. Feng and K. Müllen, *Adv. Mater.*, 2011, **23**, 3575.
15 J. Chen, Z. Wang, X. Dong, P. Chen and X. W. Lou, *Nanoscale*, 2011, **3**, 2158.
16 H. Wang, L. Xi, J. Tucek, C. Ma, G. Yang, M. K. H. Leung, R. Zboril, C. Niu and A. L. Rogach, *ChemElectroChem*, 2014, **1**, 1563.
17 H. Wang, H. Huang, C. Niu and A. L. Rogach, *Small*, 2014, **11**, 1364.
18 J. Chen, L. Yang, Z. Zhang, S. Fang and S. Hirano, *Chem. Commun.*, 2013, **49**, 2792.
19 G. Du, Z. Guo, P. Zhang, Y. Li, M. Chen, D. Wexler and H. Liu, *J. Mater. Chem.*, 2010, **20**, 5689.
20 W. Wang, Q. Sa, J. Chen, Y. Wang, H. Jung and Y. Yin, *ACS Appl. Mater. Interfaces*, 2013, **5**, 6478.
21 J. Liang, X. Yu, H. Zhou, H. B. Wu, S. Ding and X. W. Lou, *Angew. Chem., Int. Ed.*, 2014, **53**, 12803.

22 Y. Tang, Y. Zhang, J. Deng, J. Wei, H. L. Tam, B. K. Chandran, Z. Dong, Z. Chen and X. Chen, *Adv. Mater.*, 2014, **26**, 6111.
23 Y. Tang, Y. Zhang, J. Deng, D. Qi, W. R. Leow, J. Wei, S. Yin, Z. Dong, R. Yazami, Z. Chen and X. Chen, *Angew. Chem., Int. Ed.*, 2014, **53**, 1.
24 Y. Luo, J. Luo, W. Zhou, X. Qi, H. Zhang, D. Y. W. Yu, C. M. Li, H. J. Fan and T. Yu, *J. Mater. Chem. A*, 2013, **1**, 273.
25 Y. Luo, J. Luo, J. Jiang, W. Zhou, H. Yang, X. Qi, H. Zhang, H. J. Fan, D. Y. W. Yu, C. M. Li and T. Yu, *Energy Environ. Sci.*, 2012, **5**, 6559.
26 H. Kim, M. G. Kim, T. J. Shin, H. J. Shin and J. Cho, *Electrochem. Commun.*, 2008, **10**, 1669.
27 Q. Tian, Z. Zhang, L. Yang and S. Hirano, *J. Power Sources*, 2014, **253**, 9.
28 H. Park, T. Song, H. Han, A. Devadoss, J. Yuh, C. Choi and U. Paik, *Electrochem. Commun.*, 2012, **22**, 81.
29 K. Saravanan, K. Ananthanarayanan and P. Balaya, *Energy Environ. Sci.*, 2010, **3**, 939.
30 X. Wang, Z. Li, Q. Li, C. Wang, A. Chen, Z. Zhang, R. Fan and L. Yin, *CrystEngComm*, 2013, **15**, 3696.
31 X. Xu, Z. Fan, S. Ding, D. Yu and Y. Du, *Nanoscale*, 2014, **6**, 5245.